Recent Change in Summer Rainfall over the Tibetan Plateau: the Roles of External Forcing and Internal Variability

Zhaomin Ding
Chinese Academy of Meteorological Sciences

Panmao Zhai (✉ pmzhai@cma.gov.cn)
Chinese Academy of Meteorological Sciences

Renguang Wu
Zhejiang University

Research Article

Abstract

During the recent decades, summer precipitation has increased over the western and northeastern Tibetan Plateau (TP) and decreased over the southeastern TP. This study investigates the effects of external forcing and internal variability on summer rainfall changes over the TP during 1979-2013. It is shown that the variations in atmospheric circulation and precipitation over the TP are largely contributed by the anthropogenic forcing and oceanic boundary conditions and that the Interdecadal Pacific Oscillation (IPO) plays an important role in TP summer rainfall changes on decadal time scales. The sea surface temperature (SST) anomalies in the tropical central-eastern Pacific induce a wave train consisting of anomalous cyclones and anticyclones over Eurasia. The anomalous anticyclone to the northeast TP weakens westerlies, facilitating the convergence of water vapor over the TP. Further analysis indicates that the IPO-related SST anomalies contribute partly to the uncertainty in simulations of summer rainfall changes over the TP in recent decades using a 40-member ensemble of the Community Earth System Model (CESM). Consequently, the IPO can be used as one of the predictive factors of TP summer rainfall on decadal time scales.

1 Introduction

The Tibetan Plateau (TP) is known as "the Roof of the world", with a mean elevation of more than 4000m above the sea level (Xu et al. 2008). The TP contains the most glaciers outside the Arctic and Antarctic, and is referred to as "the Third Pole of the Earth" (Yao et al. 2012). The TP is also known as "the Water Tower of Asia" as it is the source region of several major Asian rivers, including the Yangtze River, the Yellow River, Brahmaputra, Mekong, Ganges, Indus, Irrawaddy and Salween, and supplies water to more than 2.0 billion people (Immerzeel et al. 2020).

The TP is one of the most sensitive regions to global climate changes and exhibits a rapid warming in recent decades along with glacier retreat and permafrost degeneration (Kuang and Jiao 2016; Yao et al. 2019). By contrast, changes in TP precipitation show larger spatial and temporal variability with lower confidence partly due to the existence of various climate regimes and complex topography (Wang et al. 2018; You et al. 2015; Zhang et al. 2017a). During 1979–2011, annual precipitation increased in most areas of the TP, but decreased in the southeastern part (Gao et al. 2015). Yang et al. (2011) obtained insignificant increasing trend in central TP and decreasing trend along the periphery for annual precipitation during 1984–2006. Liu et al. (2018) pointed out that annual precipitation decreased significantly after 1998 over the southeastern TP and increased slightly since 2002 over the northeastern TP.

The in situ rain gauge stations are mainly located in the central and eastern TP, while lakes are widely and densely distributed in the western TP (Ma et al. 2010). The majority of lakes in the northern Inner TP present an increasing expansion in the past few decades, whereas the lakes in the southern TP have shrunk (Zhang et al. 2017b, 2019a). The enhanced net precipitation is indicated to be the dominant

contributor to increased lake water storage, followed by glacier loss and permafrost degradation (Lei et al. 2019; Zhang et al. 2020).

The possible mechanism responsible for the long-term changes in TP precipitation is a great concern of the research community. Gao et al. (2014) suggested that the poleward shift of the East Asian westerly jet and the intensification of the summer monsoon circulation contribute to the general wetting trend over the TP during 1979–2011, and changes in local circulations may have played a key role in the spatially varying trends. Liu et al. (2021) indicated that the changes in moisture transport and convection activity have profound impacts on the interdecadal variations of precipitation over the northern and southern TP, respectively. Moreover, some studies found that the Atlantic multidecadal oscillation (AMO) was a key factor of summer precipitation variation over the TP on interdecadal time scales through a wave train of anomalous cyclones and anticyclones (Hu and Zhou 2021; Sun et al. 2020; Zhou et al. 2019).

Studies have been conducted to understand the change in the contribution of moisture sources to the TP precipitation (Li et al. 2019; Xu et al. 2020; Zhang et al. 2017c, 2019b). Zhang et al. (2017c) applied a Euler tracer model to analyze the water sources and revealed that the wetting trends over the central and western TP during 1979–2013 was attributable to an increased water vapor transport from the Indian Ocean and an intensification of local moisture supply. Base on a Lagrangian trajectory model, Xu et al. (2020) showed that the intensified water vapor convergence over the TP from 1979 to 2018 was attributed to the strengthened contribution from the mid-latitude westerly.

Although significant progress has been achieved in understanding the TP precipitation changes, some questions remain unclear. What are the relative contributions of external forcing and internal variability to the recent changes in TP rainfall? What is the dominant internal mode responsible for the spread in rainfall change simulations over the TP? Recently, large ensembles from a single climate model with different initial condition have become a suitable tool for identifying the relative roles of forced and internal variability in determining climate trends at regional scales (Deser et al. 2012, 2016). In this study, we aim to address the above questions using a set of large ensemble simulations.

The remainder of the paper is organized as follows. The observational datasets, model simulations, and analysis methods are described in section 2. Results are presented in section 3, including the causes of the variations of the TP summer precipitation and associated physical mechanisms. Section 4 gives the conclusions.

2 Data And Methods

2.1 Data

The in situ daily precipitation was obtained from China Meteorological Administration (CMA) for the period of 1951–2021. 133 meteorological stations located in or near the TP with less than 0.5% missing data are selected in the present analysis. Given the scarcity of meteorological stations on the western TP, two gridded precipitation datasets are applied to test the robustness of the results in this study. One is the

monthly precipitation product constructed by the Global Precipitation Climatology Center (GPCC V2018; Schneider et al. 2014), which spans from 1891 to 2016 with a horizontal resolution of 1° latitude by 1° longitude. The other is the monthly precipitation data from the China Meteorological Forced Dataset (CMFD) with a spatial resolution of 0.1°×0.1° for the period of 1979–2018 (He et al. 2020; Yang and He 2016). In addition, the ERA5 reanalysis (Hersbach et al. 2020) provided by the European Centre for Medium-Range Weather Forecasts (ECMWF) were used, including monthly precipitation, evaporation, surface pressure, specific humidity, wind velocity and geopotential height at 0.25° horizontal resolution for the time period from 1979 to the present.

We make use of monthly mean outputs from four sets of experiments conducted by the Community Earth System Model version 1 (CESM1; Hurrell et al. 2013). The first set is 10-member ensemble simulations with the atmospheric component for CESM (Community Atmospheric Model version 5 or CAM5) driven by observed sea surface temperature (SST) and sea ice conditions prescribed globally over the period of 1880–2015, termed Global Ocean Global Atmosphere (GOGA). The second set is 40-member large ensembles of fully coupled simulations with CESM (CESM-LE; Kay et al. 2015). These simulations are subject to the historical evolution of radiative forcing for 1920–2005 and the Representative Concentration Pathway 8.5 (RCP8.5) radiative forcing for 2006–2100 following the fifth phase of the Coupled Model Intercomparison Project protocols (CMIP5; Taylor et al. 2012). The third set is 20-member coupled model ensemble of tropical Pacific pacemaker simulations in which time-varying SST anomalies in the eastern tropical Pacific (10°S-10°N, 160°-90°W, with a linearly tapering buffer zone that extends to 20°S, 20°N, 180°W and the coast of South America) are restored to the model climatology plus observed historical temporal anomalies during 1920–2013. Those simulations are referred as TPAC. In the pacemaker simulations, the rest of the model's coupled climate system is free to evolve using the external forcing identical to the CESM-LE simulations. For further details of the pacemaker experiments, please refer to Deser et al. (2017). The fourth set is an 1800-year preindustrial (constant 1850 radiative conditions) control integration of the fully coupled CESM1 (Kay et al. 2015).

2.2 Method

We focus on summer season of June-July-August (JJA) and calculate linear trends by the least squares method over the period of 1979–2013. This time period was chosen because it is common in both observational datasets and model simulations. The statistical significance of long-term trends is evaluated by the nonparametric Mann-Kendall test (Mondal et al. 2012). Regression analysis is used in the present analysis. The two-sided Student's t test is used to estimate the significance of regression coefficients. The multivariate empirical orthogonal function method (MV-EOF; Wang 1992), which can capture the dominant spatial relationship among multiple variables, are used in this study. The ensemble mean (EM) of each variable is first removed from each ensemble member before the inter-member MV-EOF, and then each variable is divided by the standard deviation of that variable.

A moisture budget analysis (Chou et al. 2009; Seager et al. 2010) is employed to understand the physical processes related to the precipitation change over TP. In Chou et al. (2009), the estimated change of precipitation P' can be decomposed as:

$P' = E' - \langle V_h \nabla_h q \rangle' - \langle \omega \partial_p q \rangle' + \delta'$ (1)

where P, E, q, ω and V_h denote precipitation, surface evaporation, specific humidity, pressure velocity, and horizontal vector wind, respectively. Angel brackets denote vertical integral from the surface to tropopause, and the primes represent departures from climatological mean. δ is the residual term, which is attributed to transient eddies. The second and third terms on the right-hand side of Eq. (1) are horizontal and vertical moisture transport, respectively. The vertical moisture advection term $-\langle \omega \partial_p q \rangle'$ can be further divided as:

$$-\langle \omega \partial_p q \rangle' = -\langle \overline{\omega} \partial_p q' \rangle - \langle \omega' \partial_p \overline{q} \rangle - \langle \omega' \partial_p q' \rangle \quad (2)$$

where overbar represents climatological mean, and the first and second terms on the right-hand side of Eq. (2) are thermodynamic and dynamic components, reflecting the effects of changes in specific humidity and atmospheric circulation, respectively.

3 Results

3.1 Observed precipitation trends and related physical processes

Figure 1 exhibits the spatial distribution of TP precipitation trends in summer during 1979–2013 based on the meteorological stations, CMFD, GPCC, and ERA5 datasets. Results from all the four datasets display predominantly positive rainfall trends over the vast western TP and northeastern part of the TP, with negative trends over the southeastern TP.

To reveal the physical processes related to the TP precipitation trends, a moisture budget analysis is performed using the ERA5 reanalysis data. The spatial patterns of the trends in moisture budget components are shown in Fig. 2. A close resemblance is observed among precipitation (Fig. 1d), the vertical moisture transport term (Fig. 2d), and the dynamic component (Fig. 2f) over the TP, while the thermodynamic component displays a wetting trend (Fig. 2e). The horizontal moisture advection terms contribute partly to the increasing trend of precipitation over the northeastern TP (Figs. 2b and 2c). The drying trend of precipitation over the southeastern TP is dominated by the dynamic component related to atmospheric circulation changes. The evaporation change features a widespread decrease over the TP (Fig. 2a) possibly owing to the combined effects of decreasing net radiation and wind speed (Yao et al. 2021; Zhang et al. 2018).

Based on the above analysis, the corresponding circulation characteristics have been investigated to reveal the underlying mechanism responsible for the observed hydrological changes over the TP. The summer-mean trends in atmospheric circulation and moisture at 500hPa during 1979–2013 in ERA5 are presented in Fig. 3a. Anomalous easterly flows are seen over the TP, accompanied by increased specific humidity. It is clear that the easterly wind anomalies are generally larger to the east than to the west of the TP. Such significant contrast in wind anomalies is favorable for moisture flux convergence over the

TP (Sun et al. 2020; Zhou et al. 2019). Thus, water vapor carried by the westerlies is restrained over the TP.

Can the observed atmospheric circulation trend potentially be attributed to the observed boundary conditions over the oceans together with historical anthropogenic forcing? Indeed, much of the observed precipitation and 500hPa wind trend pattern is reproduced by the ensemble mean of the GOGA simulations (Figs. 3b and 4b). Can the observed hydroclimate trends be attributed to anthropogenic forcing? The CESM-LE ensemble mean represents an estimate of the forced response to radiative forcing. The spatial pattern of externally forced trends in precipitation and 500hPa wind (Figs. 3d and 4d) bears close resemblance to that of the ensemble mean of the GOGA (Figs. 3b and 4b) but with reduced amplitude, suggesting the combined influences of SST and anthropogenic forcing. The observed SST trend pattern resembles closely the interdecadal Pacific oscillation (IPO), and cannot be attributed to anthropogenic forcing according to the CESM-LE and other models (figures not shown). To what extent are the trends in precipitation and 500-hPa wind in GOGA EM forced by tropical Pacific SST and radiative forcing? The TPAC EM, which include both effects, also displays easterly wind anomalies over the TP but with a slightly weaker magnitude (Fig. 3c), in accordance with the weaker wetting over the central TP (Fig. 4c), compared to GOGA EM. Precipitation and atmospheric circulation responses in TPAC EM are a result of both internal variability driven by tropical Pacific SST anomalies and radiative forcing. It is noted that the simulated moisture trend (Figs. 3b-d) is much weaker than the observations (Fig. 3a), which could be related to systematic error in the model climatology over the TP (Fig. 5). The drier background in the model may limit the thermodynamic changes and in turn atmospheric circulation changes.

The above analysis suggests that the TP precipitation changes in recent decades are closely related to atmospheric circulation changes, and tropical Pacific SST changes may play an important role in the circulation changes around the TP. Hence, we will discuss the relationship between the tropical Pacific SST and TP summer rainfall changes in the subsequent analysis.

3.2 Role of tropical Pacific SST

In this section, we first examine the atmospheric teleconnection associated with the TP precipitation changes. Figure 6a shows the trend in 200-hPa eddy geopotential height in the observations. The eddy geopotential height is defined as the difference of geopotential height from its zonal mean. As can be seen in Fig. 6a, a wave train appears in the extratropics, with negative anomalies over central-eastern Atlantic Ocean and western Asia and positive anomalies over central Europe and the Lake Baikal. This large-scale wave train resembles closely the "Silk Road Pattern" (SRP). The SRP is a summer teleconnection pattern in the upper troposphere along the subtropical westerly jet over the Eurasian continent (Enomoto et al. 2003; Lu et al. 2002; Kosaka et al. 2009). This result indicates that the cyclonic circulation anomaly near the Lake Baikal is regional manifestation of SRP on the decadal time scale.

The ensemble mean of the GOGA simulations (Fig. 6b) shows a series of high pressure and low pressure systems over Eurasia but with reduced amplitude (Fig. 6a). The anomalies over North America-North Atlantic Ocean-Europe display differences from the observations. Note, however, that the anomalies

around the TP are similar to the observations. In addition, the ensemble mean of the Pacemaker simulations shows a similar pattern of geopotential height trends as GOGA EM over much of the extratropical Eurasia (Fig. 6c), indicating that the atmospheric teleconnection pattern could be forced by tropical Pacific SST anomalies. Figure 6d displays the trend in 200-hPa geopotential height from the CESM-LE EM. Although the spatial pattern is similar to that of GOGA EM, the anticyclones over the Lake Baikal and the North Pacific are much weaker (Fig. 6d).

Can the tropical Pacific SST anomalies alone reproduce the observed anomalies on decadal time scales? To address this question, we compute 35 year trends from nonoverlapping segments of the 1800 year control integration of the fully coupled CESM, for a total 51 segments. Figure 7 illustrates the trend differences in SST and 200h-Pa eddy geopotential height between the segments with SST trends averaged over 5°S-5°N, 170°-90°W below one negative standard deviation and over one positive standard deviation. The SST trend difference features a cooling in the tropical central-eastern Pacific and a warming in the western mid-latitude North Pacific (Fig. 7a), which resembles the negative phase of the IPO pattern in the observations (Dong and Dai 2015). As shown in Fig. 7b, the IPO cold phase induces a series of anticyclone and cyclone systems over the Eurasian continent at 200hPa, which is similar to the observations (Fig. 6a).

Thus, these results imply that the IPO may be one of the key internal variability modes influencing the near-term simulation of TP summer rainfall. To examine whether the IPO-related SST anomalies are responsible for the uncertainty in the simulated TP rainfall trend, the CESM1 large ensembles (CESM-LE) are used. With the same external forcing, the 40 ensemble members simulate diverse TP rainfall changes, accompanied by a variety of atmospheric circulation trend patterns (figures not shown). To identify the leading modes of the inter-member spread in TP circulation changes, the MV-EOF analysis is applied to a set of five circulation variables, including the JJA-mean 500- and 200-hPa wind vector and the 500-hPa vertical pressure velocity over the TP and adjoining regions (10°-45°N, 60°-110°E).

The first and second MV-EOF modes account for 18.4% and 12.4% of the total variance, respectively. The two leading modes can be separated from each other and from other modes based on the criterion of North et al. (1982). The regression patterns of the 500-hPa atmospheric circulation anomalies onto the normalized first principal component (PC1) show two pronounced anticyclones, with centers located to the west of TP and over eastern China, respectively (Fig. 8a). The corresponding 200-hPa non-zonal geopotential exhibits an anomalous wave train over mid- and high latitudes of Eurasia, with positive (negative) anomalies over the northwestern Europe, the east of the Caspian Sea and the eastern China (the eastern European Plain-western Siberia-Mongolia), respectively (Fig. 9a). This pattern highly resembles the typical spatial pattern of the summer North Atlantic oscillation (SNAO; Folland et al. 2009).

The general characteristics of the 500-hPa atmospheric circulation anomalies associated with the EOF2 shows an anomalous cyclone located to the west of TP and an anomalous anticyclone over the eastern China (Fig. 8b). The 200-hPa circulation anomalies associated with the EOF2 display a wave train-like teleconnection pattern along the Northern Hemisphere westerly jet, with its centers located over the high-

latitude North Atlantic, the central Europe, the Caspian Sea, the eastern China and the North Pacific (Fig. 9b). This zonal teleconnection pattern is similar to the typical pattern of the SRP.

Previous studies (Hong et al. 2017; Piao et al. 2017; Wang et al. 2017; Wu et al. 2016) have suggested that the AMO may play an import role in regulating the SRP variability on decadal time scales. However, both the EOF1 and EOF2 patterns appear to be significantly correlated with the IPO-like SST trend pattern (Fig. 10), indicating a potential link between different members of the IPO phase and the spread in the simulated TP summer rainfall in the CESM-LE. To investigate the respective contributions of SST anomalies over tropical central-eastern Pacific and western mid-latitude North Pacific to the large-scale atmospheric circulation, we compute the trend differences in 200-hPa geopotential between the realizations with SST trends averaged over 30°-60°N, 130°E-160°W (5°S-5°N, 170°-90°W) over positive 1 standard deviation and below negative 1 standard deviation in the CESM-LE. As shown in Fig. 11, the SNAO- and SRP-like atmospheric teleconnection patterns may be modulated by the SST trend anomalies over western mid-latitude North Pacific and tropical central-eastern Pacific, respectively.

4 Conclusions

In this study, the influences of external forcing and internal variability on summer rainfall changes over the TP were investigated for the years 1979–2013. During this period, the western and northeastern TP is getting wetter, while the southeastern TP becomes drier. Using the ERA5 reanalysis data, it is found that the dynamic component played a key role in rainfall changes over the TP. Climate model simulations further demonstrated that the observed trend in atmospheric circulation and precipitation could be attributed to the observed oceanic boundary conditions and anthropogenic forcing, and that the IPO was an important factor contributing to the summer precipitation changes over the TP on the decadal time scale.

The SST anomalies in the tropical central-eastern Pacific induce a wave train consisting of cyclones and anticyclones over the Eurasian continent. The anomalous anticyclone to the east of the TP causes weakened westerly winds, which reduces water vapor export on the eastern boundary and favors the convergence of water vapor over the TP. Based on a 40-member ensemble of CESM, MV-EOF analyses showed that the IPO-related SST trend anomalies contributed partly to the spread of simulated summer rainfall trends over the TP in recent decades. Therefore, the IPO could be employed as one of the predictive factors for TP summer precipitation changes on decadal time scales.

Further investigation is needed to understand the processes related to the roles of the eastern tropical Pacific SST anomalies and external forcing in inducing the SRP on the decadal time scale. Additionally, outputs from large ensemble simulations with models other than CESM are needed to examine the model dependence of the results of the present analysis.

Declarations

Availability of data and material Data used in the analysis are available on public websites.

References

1. Chou C, Neelin JD, Chen C-A, Tu J-Y (2009) Evaluating the "rich-get-richer" mechanism in tropical precipitation change under global warming. J Clim 22:1982–2005. https://doi.org/10.1175/2008jcli2471.1

2. Deser C, Knutti R, Solomon S, Phillips AS (2012) Communication of the role of natural variability in future North American climate. Nat Clim Change 2:775–779. https://doi.org/10.1038/nclimate1562

3. Deser C, Terray L, Phillips AS (2016) Forced and internal components of winter air temperature trends over North America during the past 50 Years: mechanisms and implications. J Clim 29:2237–2258. https://doi.org/10.1175/jcli-d-15-0304.1

4. Deser C, Guo R, Lehner F (2017) The relative contributions of tropical Pacific sea surface temperatures and atmospheric internal variability to the recent global warming hiatus. Geophys Res Lett 44:7945–7954. https://doi.org/10.1002/2017gl074273

5. Dong B, Dai A (2015) The influence of the Interdecadal Pacific Oscillation on temperature and precipitation over the globe. Clim Dyn 45:2667–2681. https://doi.org/10.1007/s00382-015-2500-x

6. Enomoto T, Hoskins BJ, Matsuda Y (2003) The formation mechanism of the Bonin high in August. Quart J Roy Meteor Soc 129:157–178. https://doi.org/10.1256/qj.01.211

7. Folland CK, Knight J, Linderholm HW, Fereday D, Ineson S, Hurrell JW (2009) The summer North Atlantic Oscillation: past, present, and future. J Clim 22:1082–1103. https://doi.org/10.1175/2008jcli2459.1

8. Gao Y, Cuo L, Zhang Y (2014) Changes in moisture flux over the Tibetan Plateau during 1979–2011 and possible mechanisms. J Clim 27:1876–1893. https://doi.org/10.1175/jcli-d-13-00321.1

9. Gao Y, Li X, Leung LR, Chen D, Xu J (2015) Aridity changes in the Tibetan Plateau in a warming climate. Environ Res Lett 10. https://doi.org/10.1088/1748-9326/10/3/034013

10. He J, Yang K, Tang W, Lu H, Qin J, Chen Y, Li X (2020) The first high-resolution meteorological forcing dataset for land process studies over China. Sci Data 7:25. https://doi.org/10.1038/s41597-020-0369-y

11. Hersbach H et al (2020) The ERA5 global reanalysis. Quart J Roy Meteor Soc 146:1999–2049. https://doi.org/10.1002/qj.3803

12. Hong X, Lu R, Li S (2017) Amplified summer warming in Europe–West Asia and Northeast Asia after the mid-1990s. Environ Res Lett 12. https://doi.org/10.1088/1748-9326/aa7909

13. Hu S, Zhou T (2021) Skillful prediction of summer rainfall in the Tibetan Plateau on multiyear time scales. Sci Adv 7. https://doi.org/10.1126/sciadv.abf9395

14. Hurrell JW et al (2013) The Community Earth System Model: A framework for collaborative research. Bull Am Met Soc 94:1339–1360. https://doi.org/10.1175/bams-d-12-00121

15. Immerzeel WW et al (2020) Importance and vulnerability of the world's water towers. Nature 577:364–369. https://doi.org/10.1038/s41586-019-1822-y

16. Kay JE et al (2015) The Community Earth System Model (CESM) Large Ensemble Project: A community resource for studying climate change in the presence of internal climate variability. Bull Am Met Soc 96:1333–1349. https://doi.org/10.1175/bams-d-13-00255.1

17. Kosaka Y, Nakamura H, Watanabe M, Kimoto M (2009) Analysis on the dynamics of a wave-like teleconnection pattern along the summertime Asian jet based on a reanalysis dataset and climate model simulations. J Meteorol Soc Jpn 87:561–580. https://doi.org/10.2151/jmsj.87.561

18. Kuang X, Jiao JJ (2016) Review on climate change on the Tibetan Plateau during the last half century. J Geophys Res Atmos 121:3979–4007. https://doi.org/10.1002/2015jd024728

19. Lei Y, Zhu Y, Wang B, Yao T, Yang K, Zhang X, Zhai J, Ma N (2019) Extreme lake level changes on the Tibetan Plateau associated with the 2015/2016 El Niño. Geophys Res Lett 46:5889–5898. https://doi.org/10.1029/2019gl081946

20. Li Y, Su F, Chen D, Tang Q (2019) Atmospheric water transport to the endorheic Tibetan Plateau and its effect on the hydrological status in the region. J Geophys Res Atmos 124:12864–12881. https://doi.org/10.1029/2019jd031297

21. Liu T, Yang K, Qin J, Tian FQ (2018) Construction and applications of time series of monthly precipitation at weather stations in the central and eastern Qinghai-Tibetan Plateau. Plateau Meteor 37:1449–1457. https://doi.org/10.7522/j.issn.1000-0534.2018.00060

22. Liu Y, Chen H, Li H, Zhang G, Wang H (2021) What induces the interdecadal shift of the dipole patterns of summer precipitation trends over the Tibetan Plateau? Int J Climatol 41:5159–5177. https://doi.org/10.1002/joc.7122

23. Lu R-Y, Oh J-H, Kim B-J (2002) A teleconnection pattern in upper-level meridional wind over the North African and Eurasian continent in summer. Tellus A: Dyn Meteorol Oceanogr 54:44–55. https://doi.org/10.3402/tellusa.v54i1.12122

24. Ma R, Duan H, Hu C, Feng X, Li A, Ju W, Jiang J, Yang G (2010) A half-century of changes in China's lakes: Global warming or human influence? Geophys Res Lett 37:L24106. https://doi.org/10.1029/2010gl045514

25. Mondal A, Kundu S, Mukhopadhyay A (2012) Rainfall trend analysis by Mann-Kendall test: A case study of north-eastern part of Cuttack district, Orissa. Int J Geol Earth Environ Sci 2(1):70–78

26. Piao J, Chen W, Wei K, Liu Y, Graf H-F, Ahn J-B, Pogoreltsev A (2017) An abrupt rainfall decrease over the Asian inland plateau region around 1999 and the possible underlying mechanism. Adv Atmos Sci 34:456–468. https://doi.org/10.1007/s00376-016-6136-5

27. Schneider U, Becker A, Finger P, Meyer-Christoffer A, Ziese M, Rudolf B (2014) GPCC's new land surface precipitation climatology based on quality-controlled in situ data and its role in quantifying the global water cycle. Theor Appl Climatol 115:15–40. https://doi.org/10.1007/s00704-013-0860-x

28. Seager R, Naik N, Vecchi GA (2010) Thermodynamic and dynamic mechanisms for large-scale changes in the hydrological cycle in response to global warming. J Clim 23:4651–4668. https://doi.org/10.1175/2010jcli3655.1

29. Sun J, Yang K, Guo W, Wang Y, He J, Lu H (2020) Why has the Inner Tibetan Plateau become wetter since the mid-1990s? J Clim 33:8507–8522. https://doi.org/10.1175/jcli-d-19-0471.1

30. Taylor KE, Stouffer RJ, Meehl GA (2012) An overview of CMIP5 and the experiment design. Bull Am Met Soc 93:485–498. https://doi.org/10.1175/bams-d-11-00094.1

31. Wang B (1992) The Vertical structure and development of the ENSO anomaly mode during 1979–1989. J Atmos Sci 49:698–712

32. Wang L, Xu P, Chen W, Liu Y (2017) Interdecadal variations of the Silk Road Pattern. J Clim 30:9915–9932. https://doi.org/10.1175/jcli-d-17-0340.1

33. Wang X, Pang G, Yang M (2018) Precipitation over the Tibetan Plateau during recent decades: a review based on observations and simulations. Int J Climatol 38:1116–1131. https://doi.org/10.1002/joc.5246

34. Wu B, Lin J, Zhou T (2016) Interdecadal circumglobal teleconnection pattern during boreal summer. Atmos Sci Lett 17:446–452. https://doi.org/10.1002/asl.677

35. Xu X, Lu C, Shi X, Gao S (2008) World water tower: An atmospheric perspective. Geophys Res Lett 35. https://doi.org/10.1029/2008gl035867

36. Xu K, Zhong L, Ma Y, Zou M, Huang Z (2020) A study on the water vapor transport trend and water vapor source of the Tibetan Plateau. Theor Appl Climatol 140:1031–1042. https://doi.org/10.1007/s00704-020-03142-2

37. Yang K, Ye B, Zhou D, Wu B, Foken T, Qin J, Zhou Z (2011) Response of hydrological cycle to recent climate changes in the Tibetan Plateau. Clim Change 109:517–534. https://doi.org/10.1007/s10584-011-0099-4

38. Yang K, He J (2016) China meteorological forcing dataset (1979–2015). https://doi.org/10.3972/westdc.002.2014.db. National Tibetan Plateau Data Center

39. Yao T, Thompson L, Yang W et al (2012) Different glacier status with atmospheric circulations in Tibetan Plateau and surroundings. Nat Clim Change 2:663–667. https://doi.org/10.1038/nclimate1580

40. Yao T et al (2019) Recent Third Pole's rapid warming accompanies cryospheric melt and water cycle intensification and interactions between monsoon and environment: multidisciplinary approach with

observations, modeling, and analysis. Bull Am Met Soc 100:423–444. https://doi.org/10.1175/bams-d-17-0057.1

41. Yao T, Lu H, Yu Q, Feng W, Xue Y (2021) Change and attribution of pan evaporation throughout the Qinghai-Tibet Plateau during 1979–2017 using China meteorological forcing dataset. Int J Climatol. https://doi.org/10.1002/joc.7312

42. You Q, Min J, Zhang W, Pepin N, Kang S (2015) Comparison of multiple datasets with gridded precipitation observations over the Tibetan Plateau. Clim Dyn 45:791–806. https://doi.org/10.1007/s00382-014-2310-6

43. Zhang W, Zhou T, Zhang L (2017a) Wetting and greening Tibetan Plateau in early summer in recent decades. J Geophys Res Atmos 122:5808–5822. https://doi.org/10.1002/2017jd026468

44. Zhang G, Yao T, Shum CK et al (2017b) Lake volume and groundwater storage variations in Tibetan Plateau's endorheic basin. Geophys Res Lett 44:5550–5560. https://doi.org/10.1002/2017gl073773

45. Zhang C, Tang Q, Chen D (2017c) Recent Changes in the moisture source of precipitation over the Tibetan Plateau. J Clim 30:1807–1819. https://doi.org/10.1175/jcli-d-15-0842.1

46. Zhang C, Liu F, Shen Y (2018) Attribution analysis of changing pan evaporation in the Qinghai-Tibetan Plateau, China. Int J Climatol 38:e1032–e1043. https://doi.org/10.1002/joc.5431

47. Zhang G, Luo W, Chen W, Zheng G (2019a) A robust but variable lake expansion on the Tibetan Plateau. Sci Bull 64:1306–1309. https://doi.org/10.1016/j.scib.2019.07.018

48. Zhang C, Tang Q, Chen D, van der Ent RJ, Liu X, Li W, Haile GG (2019b) Moisture source changes contributed to different precipitation changes over the northern and southern Tibetan Plateau. J Hydrometeorol 20:217–229. https://doi.org/10.1175/jhm-d-18-0094.1

49. Zhang G, Yao T, Xie H, Yang K, Zhu L, Shum CK, Bolch T, Yi S, Allen S, Jiang L, Chen W, Ke C (2020) Response of Tibetan Plateau lakes to climate change: Trends, patterns, and mechanisms. Earth Sci Rev 208. https://doi.org/10.1016/j.earscirev.2020.103269

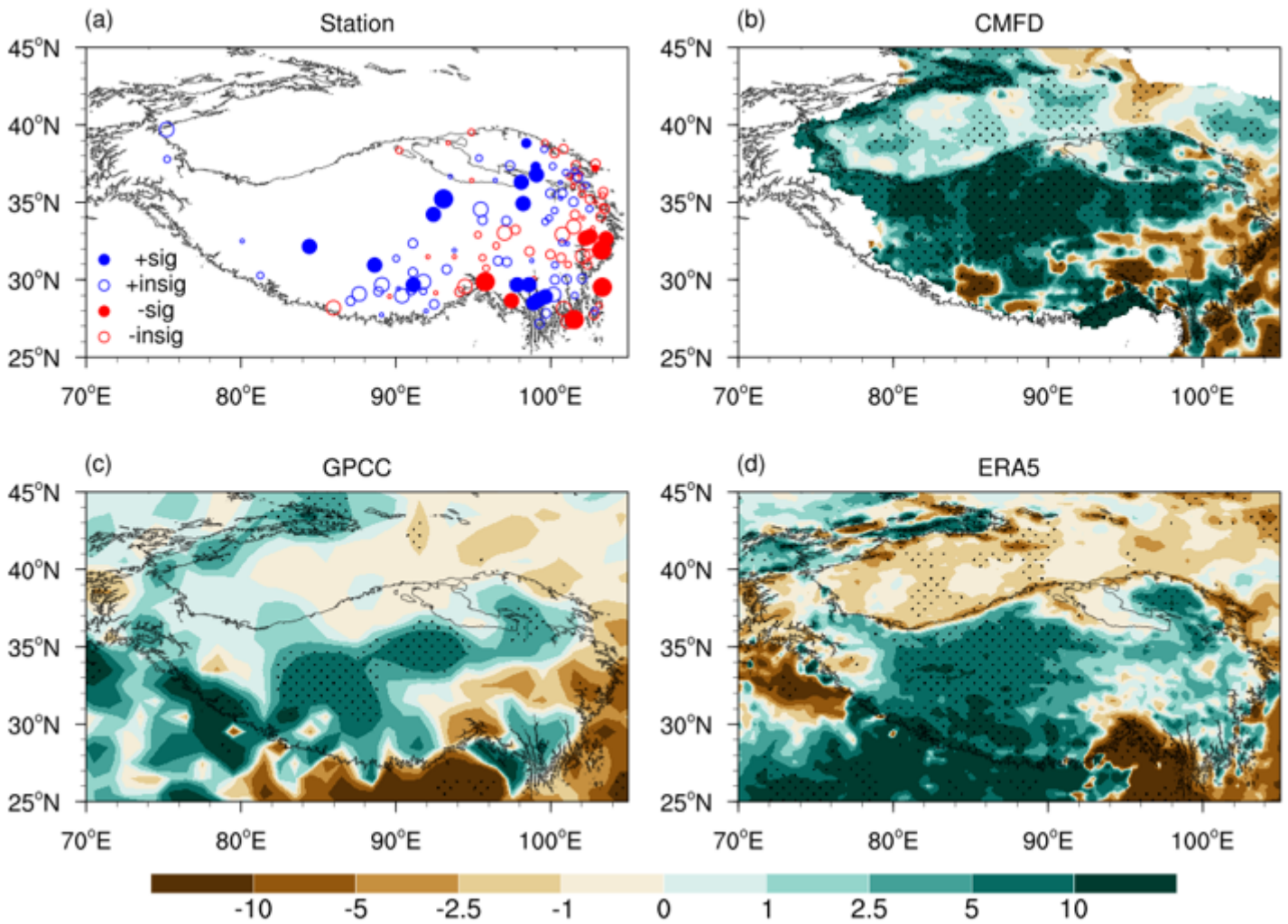50. Zhou C, Zhao P, Chen J (2019) The interdecadal change of summer water vapor over the Tibetan Plateau and associated mechanisms. J Clim 32:4103–4119. https://doi.org/10.1175/jcli-d-18-0364.1

51. Zhou C, Zhao P, Chen J (2019) The interdecadal change of summer water vapor over the Tibetan Plateau and associated mechanisms, J Clim 32:4103–4119. https://doi.org/10.1175/jcli-d-18-0364.1

Figures

Figure 1

Observed precipitation trends over Tibetan Plateau in summer. The precipitation trends (mm month^{-1} decade^{-1}) during 1979-2013 derived from (a) station observations, (b) CMFD, (c) GPCC and (d) ERA5. The stippling denotes the linear trend significant at the 10% confidence level according to the MK test. Blue dots indicate wetting trends and red dots indicate drying trends. Solid dots denote trends significant at the 10% confidence level according to the MK test. The black lines show the 3000-m contour line of the TP.
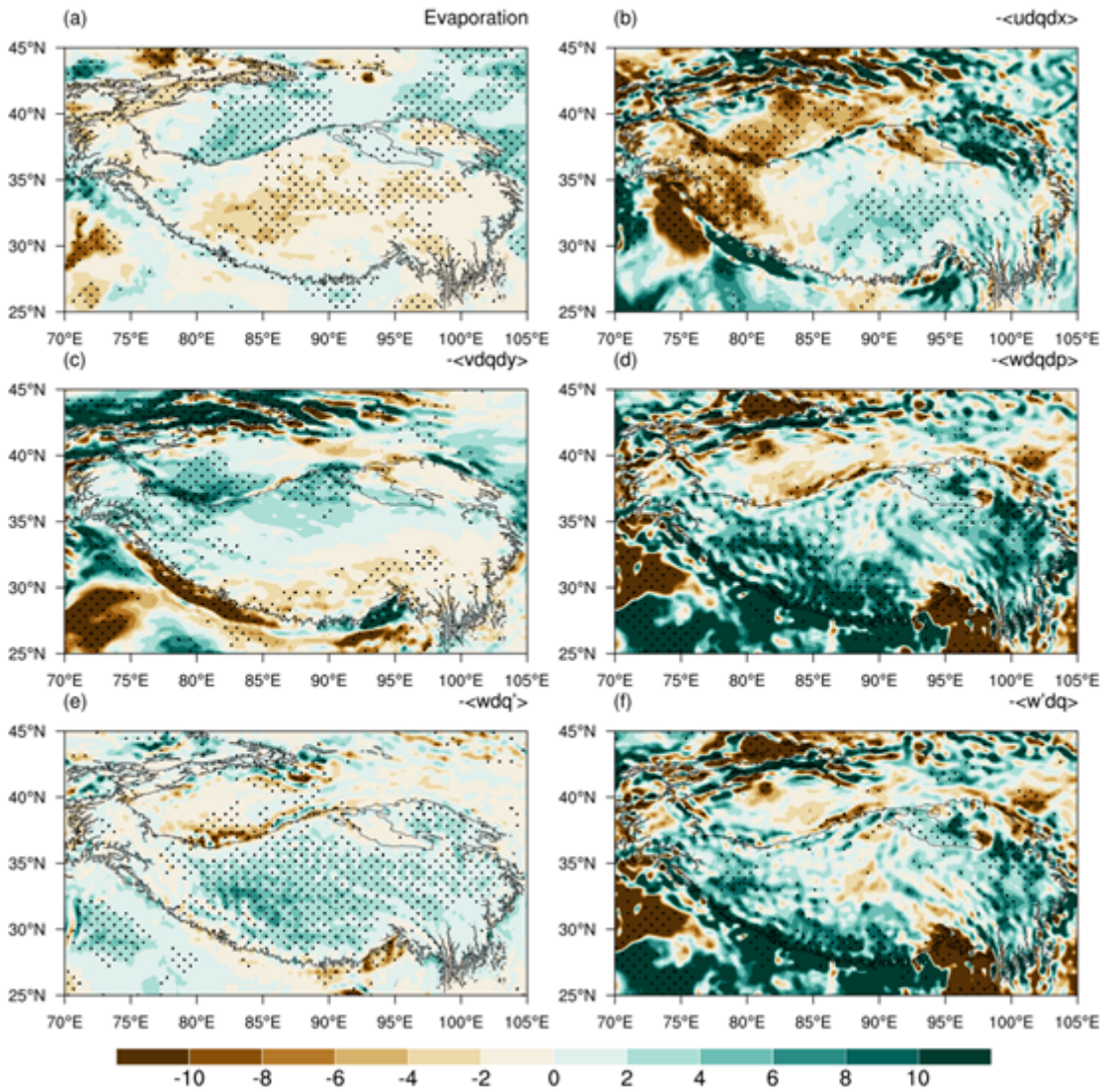
Figure 2

Linear trends of the moisture budget terms over Tibetan Plateau in summer during 1979-2013 derived from ERA5. The linear trends (mm month^{-1} decade^{-1}) of (a) evaporation, (b) the zonal advection term, (c) the meridional advection term, (d) the vertical advection term, and the (e) thermodynamic and (f) dynamic components of the vertical advection term. The stippling denotes the linear trend significant at the 10% confidence level according to the MK test.
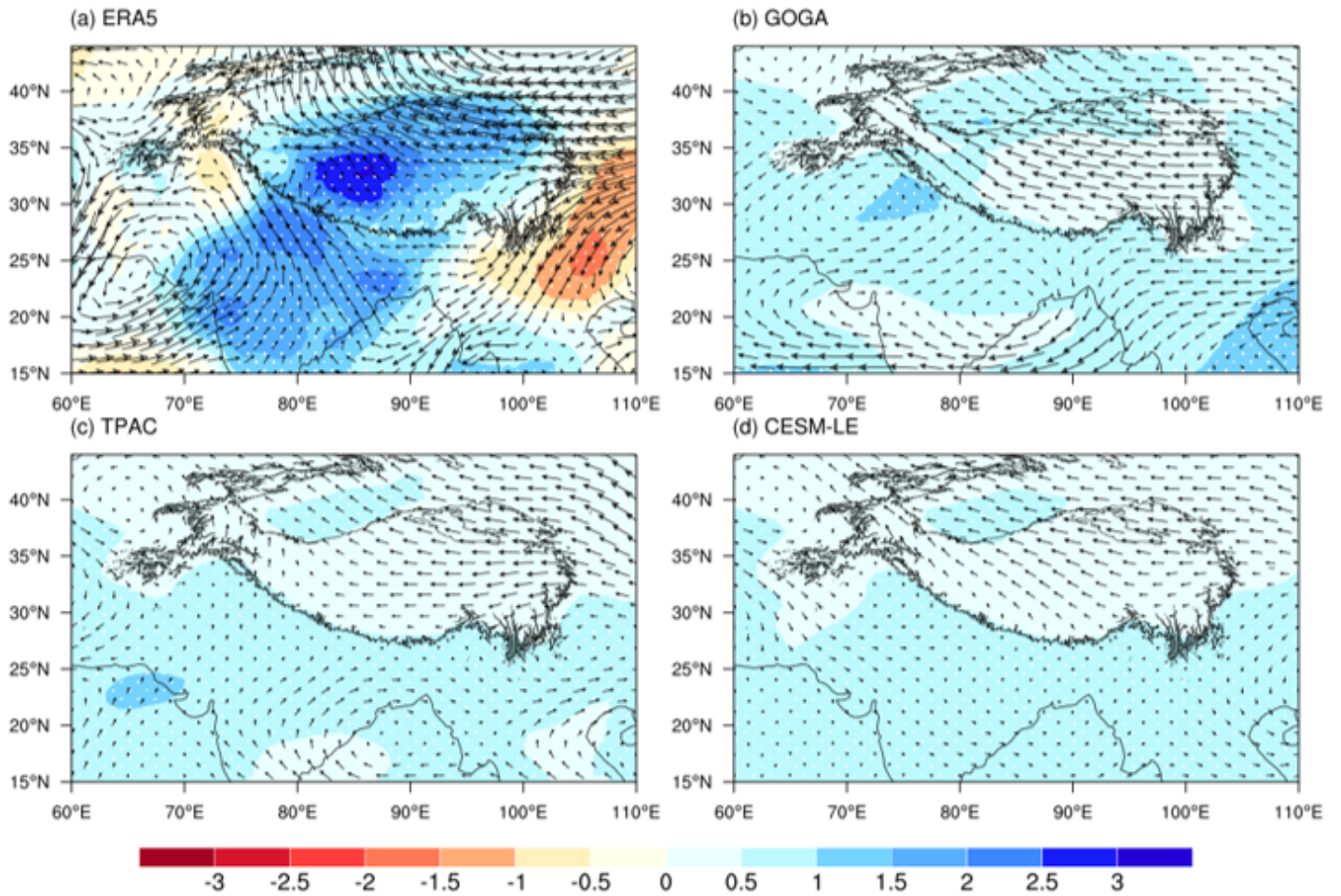
Figure 3

Linear trends in specific humidity (shaded; 10^{-4} kg/kg/decade) and wind (vectors; m/s/ decade) at 500hPa over the Tibetan Plateau in summer during 1979-2013 in (a) ERA5, (b) GOGA ensemble mean, (c) TPAC ensemble mean, and (d) CESM-LE mean. The stippling denotes the linear trend significant at the 10% confidence level according to the MK test.
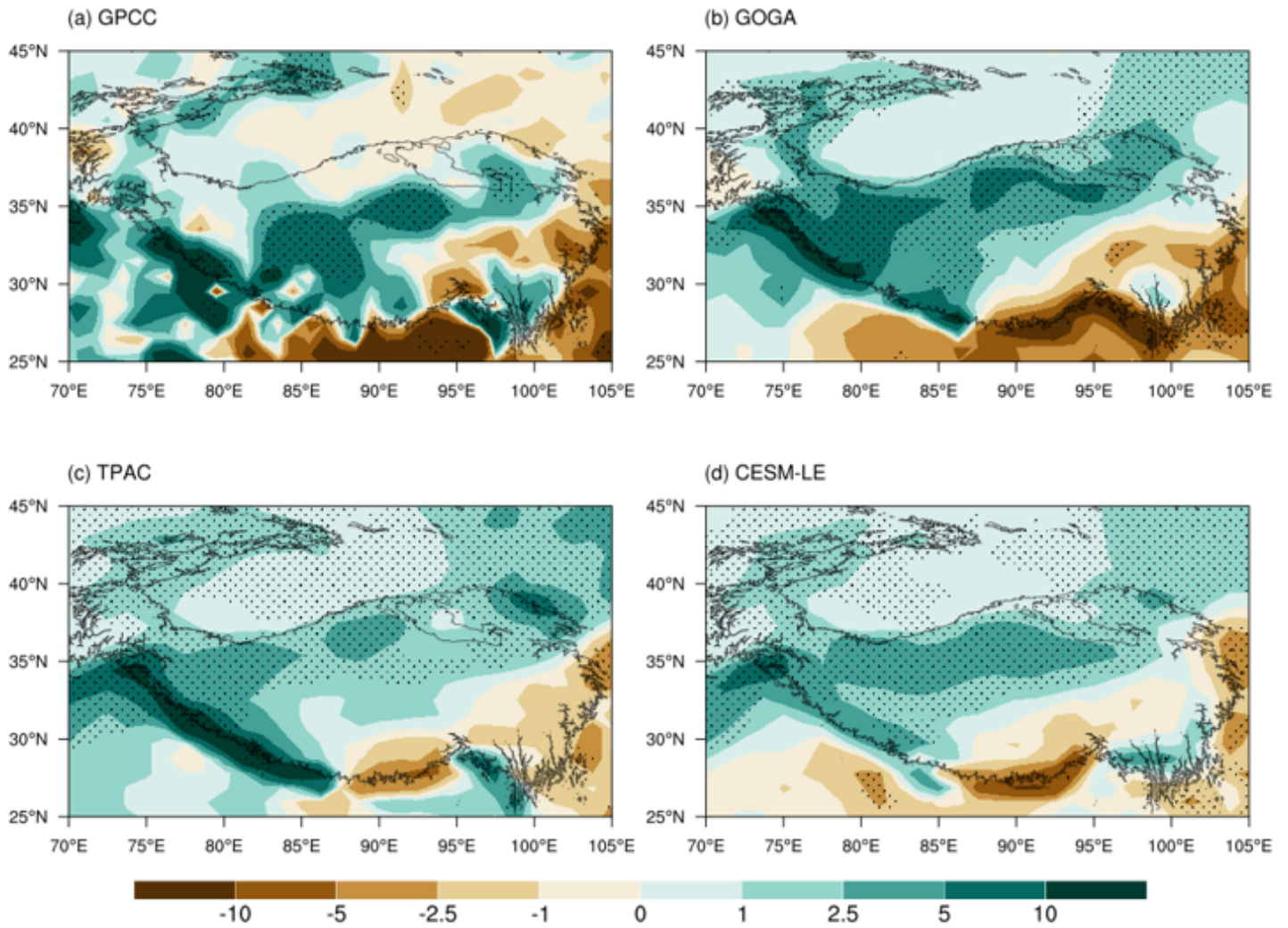
Figure 4

Summer precipitation trends (mm month^{-1} decade^{-1}) over Tibetan Plateau from 1979 to 2013 in (a) GPCC, (b) GOGA ensemble mean, (c) TPAC ensemble mean, and (d) CESM-LE mean. The stippling denotes the linear trend significant at the 10% confidence level according to the MK test. Note that Fig. 4a is the same as Fig. 1c.
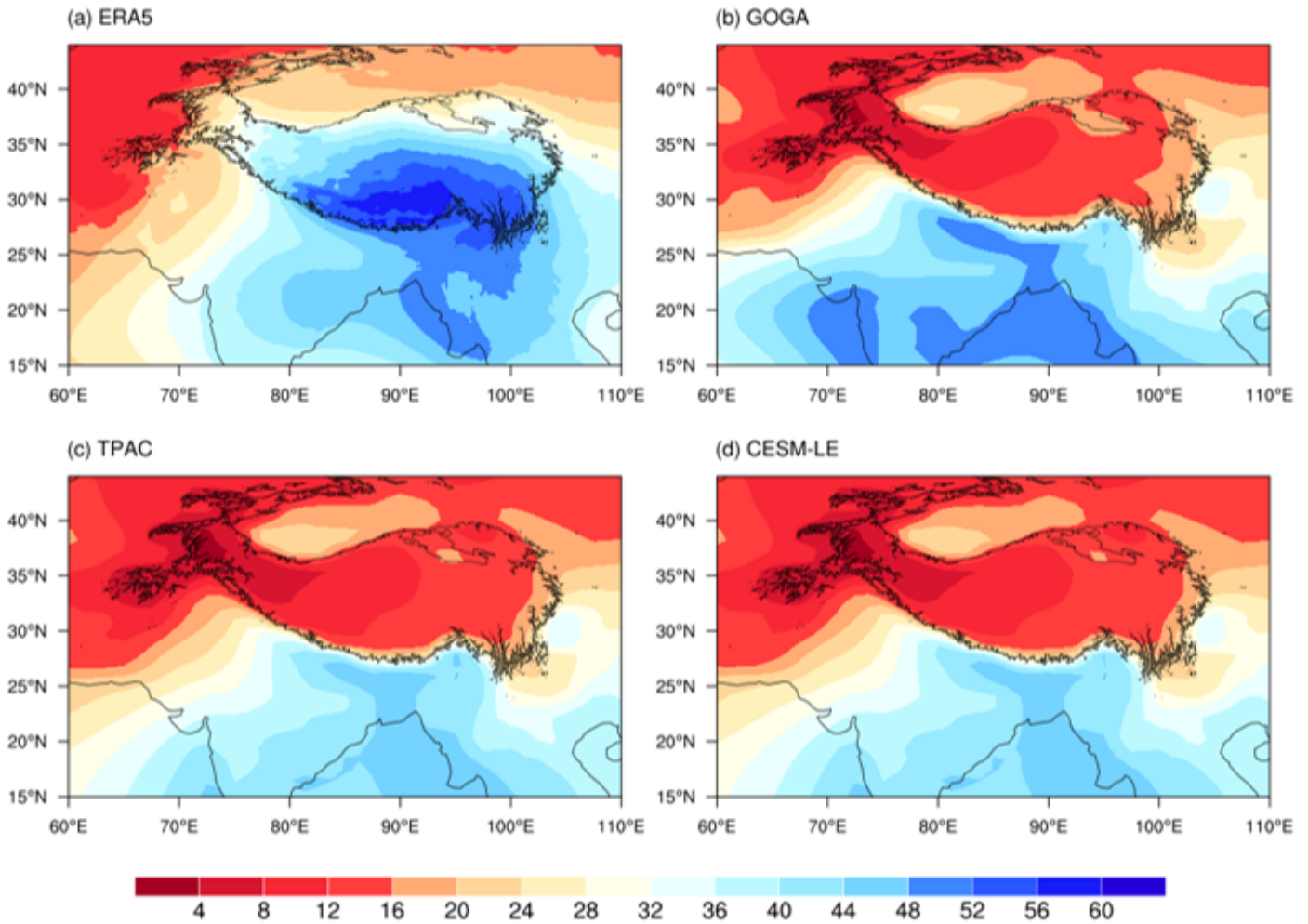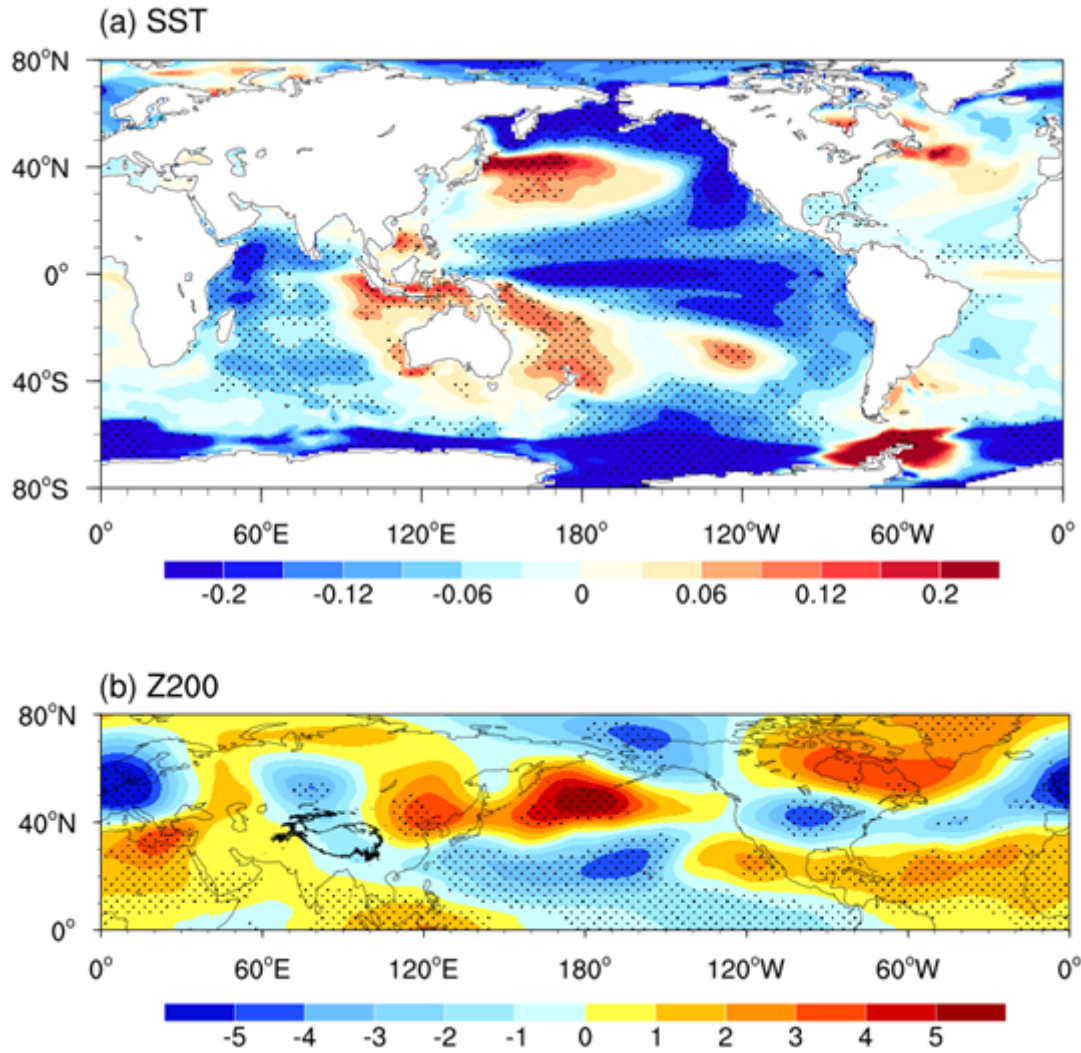
Figure 5

Climatology of summer specific humidity (10^{-4} kg/kg/) at 500hPa over Tibetan Plateau for 1979-2013 constructed from the (a) ERA5 reanalysis, (b) GOGA ensemble mean, (c) TPAC ensemble mean, and (d) CESM-LE mean.
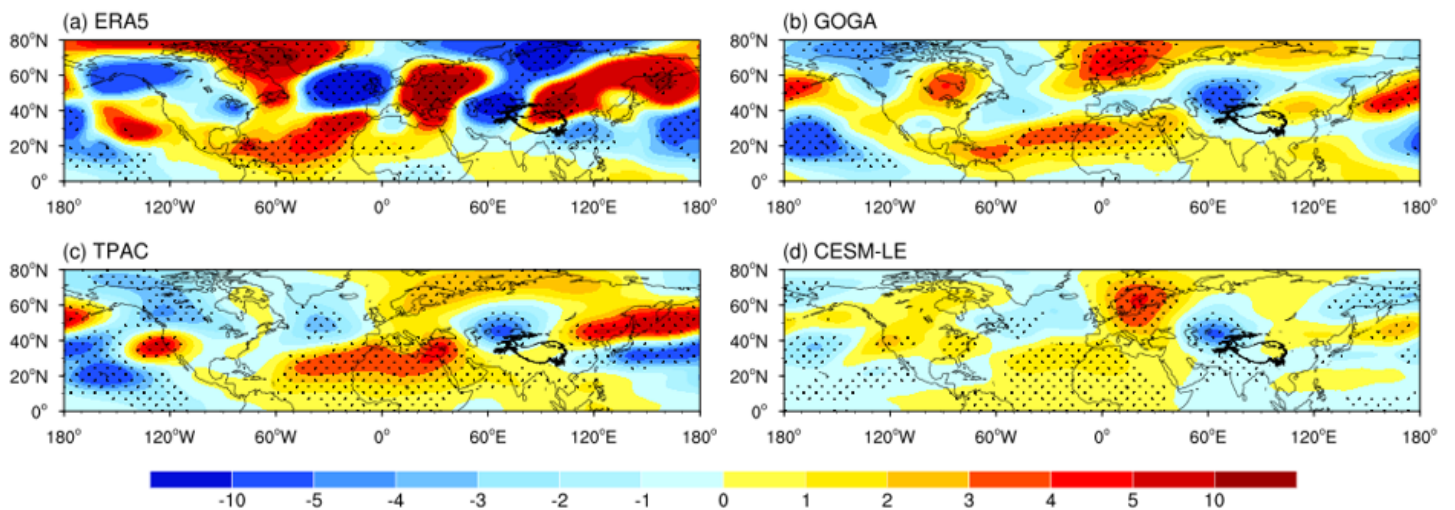
Figure 6

Linear trends (m/decade) of summer non-zonal geopotential height at 200hPa over Tibetan Plateau during 1979-2013 in the (a) ERA5 reanalysis, (b) GOGA ensemble mean, (c) TPAC ensemble mean, and (d) CESM-LE mean. The stippling denotes the linear trend significant at the 10% confidence level according to the MK test.

(a) SST

(b) Z200

Figure 7

The differences of 35 year trends in (a) SST (°C/decade) and (b) non-zonal geopotential height (m/decade) at 200hPa in summer for the SST trends averaged over 5°S-5°N, 170°-90°W between below one negative standard deviation and over one positive standard deviation (the former minus the latter) from the PiCTL. The dotted areas indicate that differences are significant at the 0.1 confidence level according to the Student's *t* test.
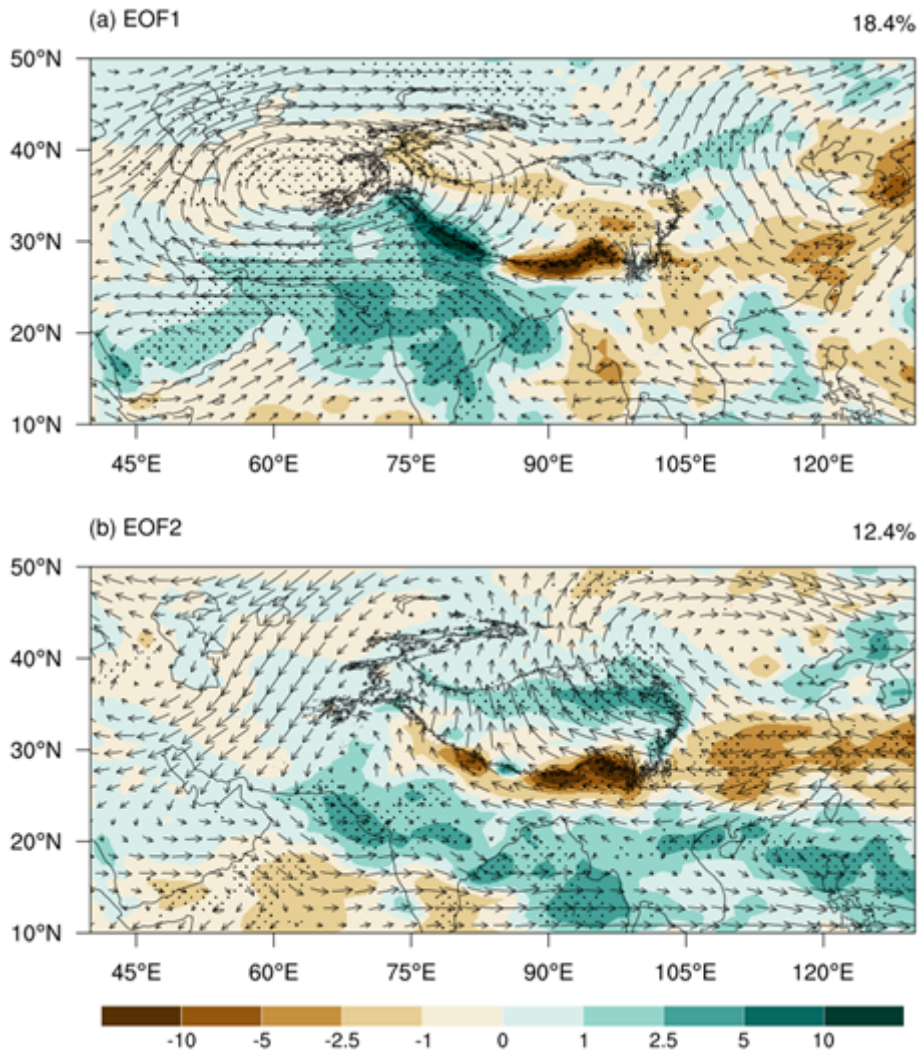
Figure 8

Inter-member regressions of trends in rainfall (shaded; mm month^{-1} decade^{-1}) and 500-hPa winds (vectors; m s^{-1} decade^{-1}) in summer during 1979-2013 onto the normalized principal component of the (a) first and (b) second MV-EOF modes from the CESM-LE. Stippling indicates the regressions are significant at the 0.1 level based on the Student's t test.
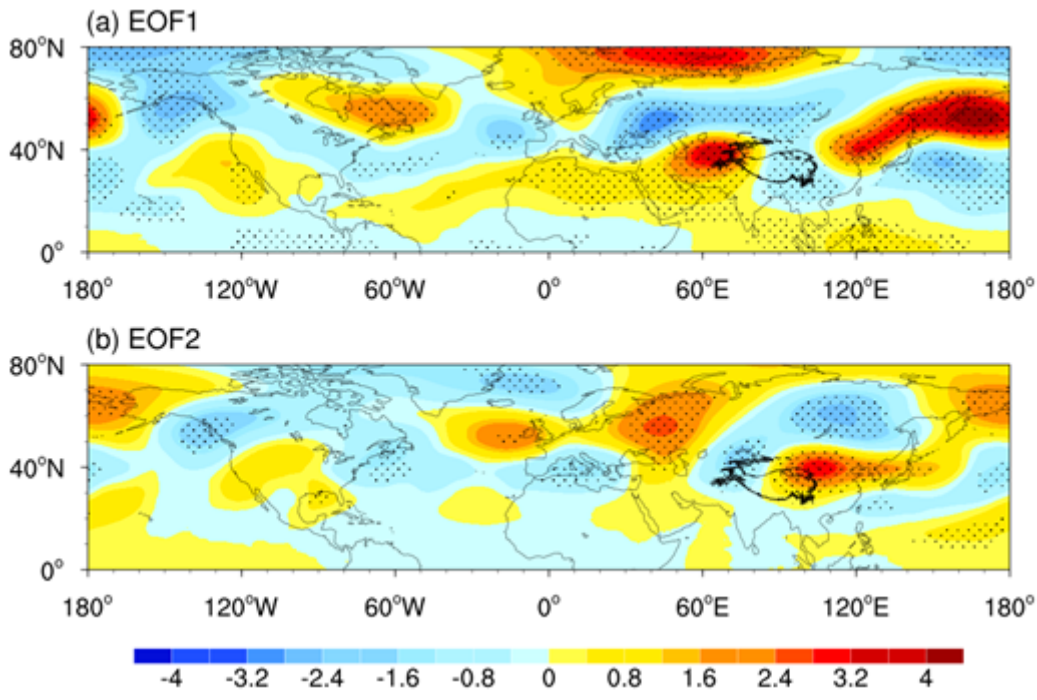
Figure 9

As in Fig. 8 but for trends in non-zonal geopotential height (m decade^{-1}).
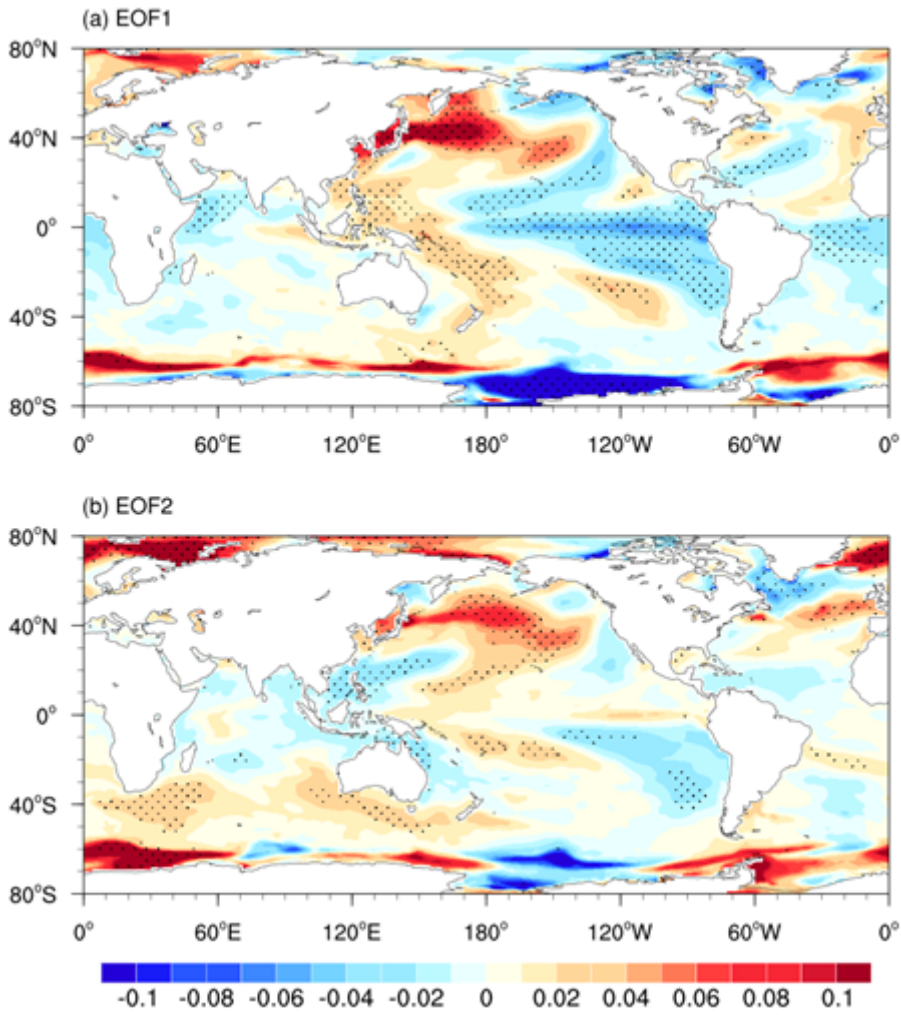
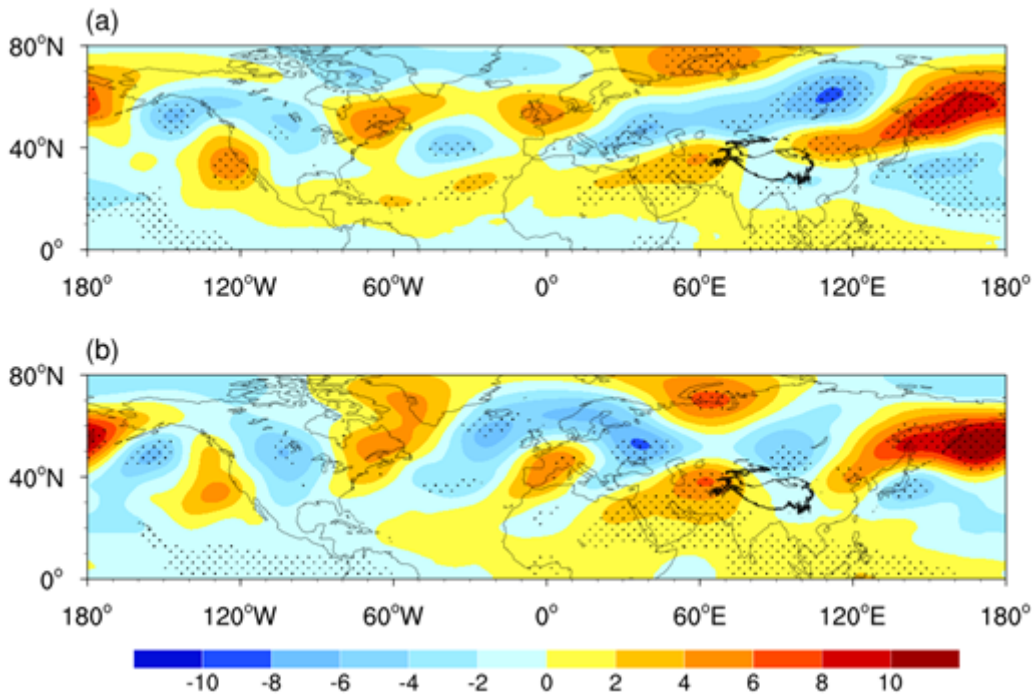**Figure 10**

As in Fig. 8 but for trends in SST (˚C decade⁻¹).

Figure 11

The differences of trends in non-zonal geopotential height (m/decade) at 200hPa in summer during 1979-2013 for the SST trends (°C/decade) averaged over (a) 30°-60°N, 130°E-160°W and (b) 5°S-5°N, 170°-90°W between over one positive standard deviation and below one negative standard deviation (the former minus the latter and the latter minus former, respectively) from the CESM-LE. The dotted areas indicate that differences are significant at the 0.1 confidence level based on the Student's *t* test.